

PAPER

Single-shot low coherence pointwise measuring interferometer with potential for in-line inspection

To cite this article: R Hahn *et al* 2017 *Meas. Sci. Technol.* **28** 025009

View the [article online](#) for updates and enhancements.

Related content

- [Reduction of chromatic aberration influences in vertical scanning white-light interferometry](#)
Peter Lehmann, Peter Kühnhold and Weichang Xie
- [Low coherent Linnik interferometer optimized for use in nano-measuring machines](#)
Jan Niehues, Peter Lehmann and Weichang Xie
- [White-light interferometers with polarizing optics for length measurements with an applicable zero-point detection](#)
V Ullmann, S Emam and E Manske

Single-shot low coherence pointwise measuring interferometer with potential for in-line inspection

R Hahn, J Krauter, K Körner, M Gronle and W Osten

Institut für Technische Optik, Universität Stuttgart, Pfaffenwaldring 9, D-70569 Stuttgart, Germany

E-mail: hahn@ito.uni-stuttgart.de

Received 10 October 2016, revised 28 November 2016

Accepted for publication 9 December 2016

Published 29 December 2016



Abstract

Low-coherence-interferometry (LCI) is a well-known optical metrology technique which offers high resolution and a low measurement uncertainty. For the inspection of dynamic and fast processes, single-shot point sensors can show their full capability. Therefore, a new approach of an interferometer is presented, allowing an single-shot acquisition of a LCI signal. The presented concept is based on tilted wavefronts to generate a spatial modulated interferogram. Using a three faceted mirror (TFM) in the reference path, a virtual field point is generated leading to a tilted planar reference wavefront in the pupil plane of the telecentric objective lens. Three mirror surfaces, which are diamond milled out of a monolithic copper cube, are applied to guarantee a stable TFM geometry, resulting in an invariant reference field point position.

Keywords: metrology, optical design of instruments, fringe analysis, mirror system design, mirrors, optical devices, interferometry

(Some figures may appear in colour only in the online journal)

1. Introduction

For the fabrication of modern technical products, high quality has to be guaranteed despite the continuously increasing quantities. For quality control, sensors providing high resolutions, low measurement uncertainties and a high robustness are needed [1]. However, the speed of the signal acquisition can be a strongly limiting factor for the application of optical sensors, especially for in-line inspection tasks. Single shot sensors are appropriate approaches to provide fast and dynamic height measurements. Besides spectral-interferometry (SI) [2–4], white-light-interferometry (WLI) turns out to be a convenient method for measurement tasks with high demands on axial and lateral resolution down to the nanometer range [5–7].

In Endo *et al* [4], a SI single-shot line sensor is demonstrated, whose approach is the optical splitting by a grating along only one lateral axis. So one camera axis observes the interferograms corresponding to the lateral object positions of the illuminated line. A measurement of a coin is shown with

a resolution in the micrometer range due to the Fourier-based signal evaluation. A known approach for a LCI single-shot line profiling sensor is a Linnik–Mach–Zehnder interferometer combination with a tilted mirror in the reference path, which however seems to be a rather unstable arrangement caused by the high number of optical elements [8–10]. Another point sensor approach uses a second miniaturized Michelson interferometer with a tilted reference mirror after a fiber-optical Fizeau-interferometer [11]. The interference contrast of this system is significantly reduced by the two interferometer stages. Also, there is no possibility to scan one line of the object in one shot due to fiber architecture.

To make the non-scanning LCI more attractive, we want to present a more robust setup for a fast interferometric point sensor, combining the advantages of the mentioned systems. First, the sensor concept is introduced, followed by the sensor design and tolerancing. In a further section, the signal processing is demonstrated by a real data set and finally a first measurement example of a depth calibration standard is shown.

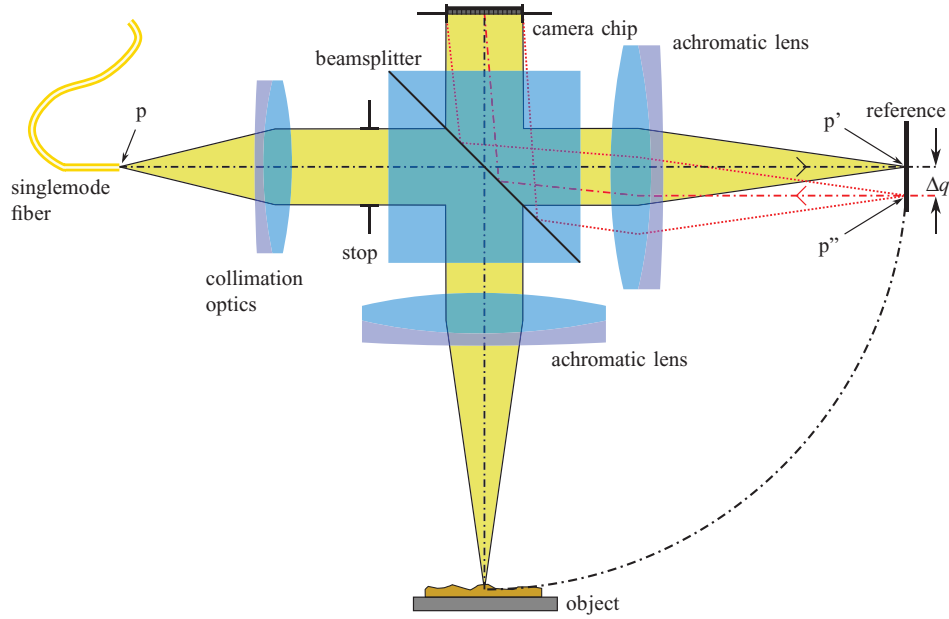


Figure 1. Concept of the single-shot WLI with a fiber, collimation optics, a beamsplitter, two objective lenses for the Linnik-interferometer and a camera detector. In the reference path the virtual field is indicated (dotted line) with a lateral shear of Δq .

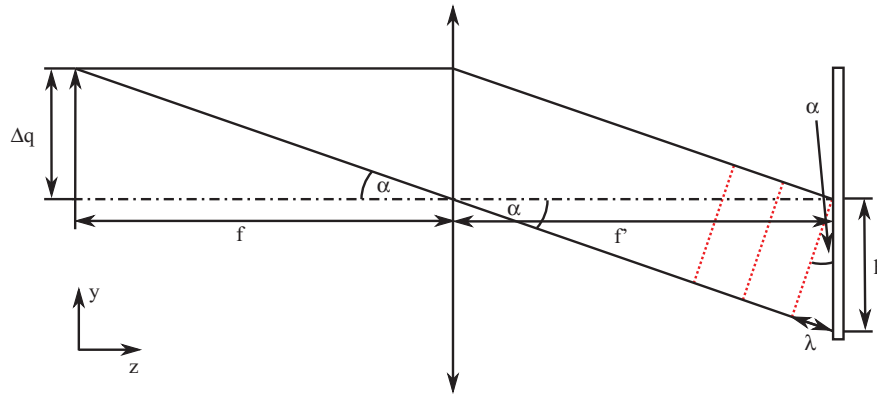


Figure 2. Geometric relationship between the lateral shear Δq , the lens focal length f , fringe period h and the tilt angle α .

2. Sensor concept

Körner *et al* [12] proposes a WLI for the robust metrology of technical surfaces. All known single-shot WLI systems need a phase-wedge between the object and reference wavefront to generate a spatial modulated interferogram which is completely detected in one camera frame. This is usually done by inserting a slight tilt between the two wavefronts by means of a tilted reference mirror [8, 9, 11]. In the presented setup, the tilt is obtained by introducing a virtual field point in the reference arm (see figure 1). After the collimation of this point by a telecentric objective lens, the reference wavefront has a defined tilt angle with respect to the optical axis. The purposed mirror element is introduced in section 3.1.

As schematically drawn in figure 1, a broadband superluminescent diode (SLD) is coupled into the setup by a singlemode fiber. After collimating the light coming from the fiber end point p , it is split into the reference and the object arm by a beamsplitter cube. An interferometer in the Linnik configuration with two equal achromatic lenses is used. The system

aperture stop is placed in the back focal plane of the lenses to achieve a telecentric object and reference space. In the object path the light is focused onto the object and after reflecting it is collimated again and propagates then as a plane wavefront towards the detector. In the reference arm, the light focused at the point p' is reflected back with a laterally displaced distance Δq , using a mirror combination in order to keep the chief rays parallel to the optical axis. Caused by this lateral displacement, a coherent virtual field point p'' for the reference is generated which results in a planar, tilted wavefront after the collimation.

The geometric drawing in figure 2 shows the relationship between the tilt angle α , the focal length f and the lateral shear Δq .

The angle α is defined by:

$$\alpha = \arctan\left(\frac{\Delta q}{f}\right). \quad (1)$$

With the use of α , the wave vector \mathbf{k}_R can be expressed by:

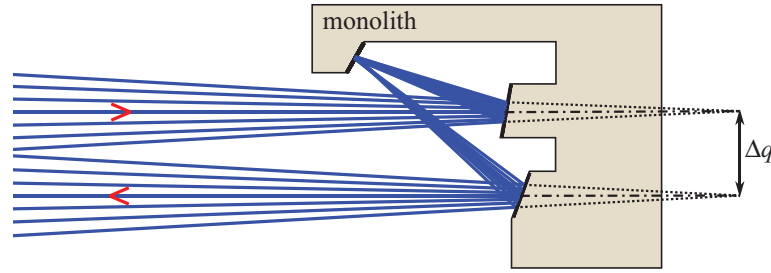


Figure 3. TFM, optimized by the software ZEMAX, leading to a lateral shear Δq . The dotted lines show the virtual focal positions of the incoming and outgoing ray bundles.

$$\mathbf{k}_R = \frac{2\pi}{\lambda} \begin{pmatrix} \cos(\alpha) \\ -\sin(\alpha) \end{pmatrix}. \quad (2)$$

Whereas the wave vector of the object beam \mathbf{k}_O is defined by:

$$\mathbf{k}_O = \frac{2\pi}{\lambda} \begin{pmatrix} 1 \\ 0 \end{pmatrix}. \quad (3)$$

The electric field strengths of the wavefields in dependency on the location \mathbf{p} are generally given by:

$$\begin{aligned} E_R &= A_R \times \exp(i\mathbf{k}_R \cdot \mathbf{p}) \\ E_O &= A_O \times \exp(i\mathbf{k}_O \cdot \mathbf{p}), \end{aligned} \quad (4)$$

with:

$$\mathbf{p} = \begin{pmatrix} z \\ y \end{pmatrix} \quad (5)$$

and the field amplitudes A_R and A_O . After the superposition of the field E_R and E_O at the observation plane ($z = 0$), one can find the interference intensity for one wavelength as a function of y :

$$\begin{aligned} I(y) &= |E_R + E_O|^2 = I_R + I_O + 2(I_R I_O)^{1/2} \\ &\quad \cos\left[-\frac{2\pi}{\lambda} \sin(\alpha) \times y\right], \end{aligned} \quad (6)$$

with the intensities I_R and I_O of the reference and object arm. The fringe period h in the observation plane is defined by the expression:

$$h = \frac{\lambda}{\sin(\alpha)}. \quad (7)$$

By combining equations (1) and (7) the lateral shear Δq is given as:

$$\Delta q = \tan\left[\arcsin\left(\frac{\lambda}{h}\right)\right] \times f. \quad (8)$$

If the optical system is telecentric in the object space, the rear focal plane of the objective lens is the pupil plane of the optical system. The superposition area of the wavefronts is at the maximum at this plane. Then the theoretical measurement range Δz_{\max} can be calculated with the pupil diameter d_{pupil} and center wavelength λ_0 of the lightsource spectrum which defines the signal's frequency of a LCI interferogram (see also equation (14)):

$$\Delta z_{\max} = \frac{d_{\text{pupil}} \times \lambda_0}{2h}. \quad (9)$$

Here d_{pupil}/h gives the maximally observable number of fringes on the sensor, while the factor $\frac{1}{2}$ is needed to compensate the fact that each beam has to propagate twice through the respective arm of the interferometer.

3. Sensor design

To realize the previously presented sensor, a carefully elaborated optical design is needed. A possible solution which was realized in a laboratory setup, is presented in the following. First the realization of the mirror optics which is the key component of the new sensor concept is described, followed by some tolerancing and the design of the whole sensor.

3.1. Parallel shear of the ray bundle with the use of mirror optics

A stable lateral shear of the reference beam is the crucial point of the functionality of the single-shot LCI sensor. As discussed in chapter 2, the lateral shear distance Δq defines the tilt angle α of the reference wavefront in the pupil plane and therefore, the observable fringe period h at the detector, as well as the maximal axial measurement range Δz_{\max} . For the illumination of the system, a fiber-coupled SLD with a central wavelength of $\lambda_0 \approx 850$ nm and a bandwidth of $\Delta\lambda \approx 40$ nm is used. To keep the design of the mirror group as simple as possible a long focal length for the lenses is chosen with $f = 100$ mm. A XIMEA camera with a square CMOSIS chip featuring a edge length of 11.27 mm, 2048×2048 pixels and a pixel pitch of $5.5 \mu\text{m}$ is used. With respect to equation (8), Δq must be 1.54 mm in order to guarantee a convenient sampling of 10 pixels/period.

An appropriate manner to realize the shear is the use of a mirror group with an odd number of reflections, such that no overall lateral inversion of the wavefront is induced by the entire set of odd mirror surfaces [13]. This is important to guarantee a high interference contrast in the signal. Another advantage of the odd number of reflections is the invariance of Δq when the mirror group is moved in lateral direction. Figure 3 shows the designed mirror optics with three reflecting surfaces of a monolith. The design of this reflector has been

done by using the Software ZEMAX. The most important criteria was to avoid vignetting effects caused by mirror surfaces in the beam path, while the optical path length difference (OPD) of both arms has to be zero.

In the laboratory setup, the fabricated TFM generates a lateral shear of $\Delta q = 1.57$ mm which leads to a measured fringe period of $h = 54$ μm such that one period is sampled by 9.78 pixels. This causes a theoretical measurement range of $\Delta z_{\text{max}} = 87.08$ μm . The TFM was made out of a monolithic copper cube by the company LT ULTRA [14], as shown in figure 4. Copper as mirror material was given by the company due to its manufacturing process.

The size is $7 \times 7.5 \times 100$ mm with a smallest mirror height of 0.6 mm, a total shape accuracy smaller than 0.25 μm and a surface roughness less than 6 nm R_a . The significant advantage of the monolithic fabrication is the stiffness of the mirror group, leading to a high robustness against external influences like vibrations.

3.2. Comparison of suitable mirror geometries

In the following, a simulative comparison between the behavior of the proposed TFM and a hollow roof mirror (HRM) will be given. A HRM produces a lateral shear but also a lateral inverted wavefront, what yields to a low contrast in the interference signal. Nevertheless, it is chosen as a comparable mirror geometry due to low complexity. For simplicity, the reflection by a HRM and a TFM of a single ray is schematically shown in figure 5.

If a ray hits the HRM, it is reflected back in parallel direction with a lateral shear distance Δq_1 . If the same incoming ray hits the HRM at a different y position, the ray is reflected with a different lateral shear distance Δq_2 . In case of the TFM, the lateral shear is independent of the y position of the reflector and remains constant for both incoming rays ($\Delta q_1 = \Delta q_2$). This can be validated in a simulative comparison, where the mirror optics have been displaced in the lateral direction by ± 0.2 mm. On the one hand, in case of the HRM, the fringe sampling on the camera varies between 8.3 pixel and 11.9 pixel (see figure 6(a)). On the other hand, the sampling as well as the lateral shear Δq remains constant for all lateral positions of the TFM (see figure 6(b)).

Another positive effect of the TFM is the variation of the sampling when the reflector is tilted. In the following simulative comparison the TFM and the HRM have been tilted by $\pm 2^\circ$ around the first contact point of the chief ray with the mirror group. This has been done for several axial positions of the mirror optics, starting with a system having an OPD equal to zero. The result is depicted in figure 7. It can be seen that the variation of the sampling for the HRM varies between 9.45 and 10.15 pixel for different tilt angles. The dependency on the tilt angle for the TFM is less and varies between 9.65 and 9.85 pixel.

For a robust object height evaluation, it is important to ensure a constant frequency of the fringe pattern on the detector, but also to avoid variations of the OPD which can for instance be caused by a tilt of the mirror optics. Similar to the analysis before, the influence by the tilt of the reflectors on the

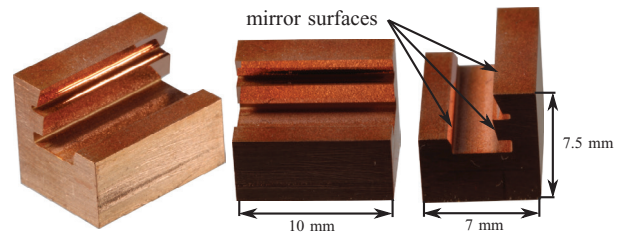


Figure 4. Monolithic copper TFM, fabricated by LT ULTRA.

resulting OPD has been simulated and is shown in figure 8. The different lines show the OPD behavior for different axial positions of the reference mirror group. For all simulated cases, the slopes of the curves are equal, so that the variation of the OPD is constant for all axial positions. However, the comparison between corresponding axis positions of the HRM and TFM simulations show, that in this case the absolute variation of the OPD is less when the HRM is used.

The result in figure 8 will be different for other tilt axes and combinations of them, like they would exist in a vibrating environment. Bauerschmidt investigated the behavior of different mirror series by any spatial displacement in an analytic way [13]. He also showed that there is a reference tilt position for a mirror series without changing the path length. All these simulations above are giving a first *qualitative* impression of the system behavior.

3.3. Laboratory setup

In the following, as schematically depicted in figure 1, the laboratory setup with the previously presented TFM is discussed. The system only provides the full theoretical measurement range, when the camera chip is fully illuminated. Therefore, the collimating lens has to be adapted to the numerical aperture (NA) of the fiber. The realized system uses an achromatic lens with a focal length of 60 mm for collimation. This focal length is longer than the one needed to achieve a more homogeneous illumination of the pupil. Due to the design of the TFM it is necessary to choose a focal length of the objective lens longer than 100 mm, otherwise vignetting effects will appear by the mirror surfaces. The long focal length leads into a NA of about 0.054, which results in a long depth of focus, so that the axial measurement range is not limited by the NA. Nevertheless, the low NA limits the lateral resolution and the maximal detectable flank angle of an object. In order to keep the system as simple as possible, spherical achromatic lenses are used. Despite the simplicity of the optical elements, the illumination of the object is still diffraction limited.

4. Signal processing and verification

All interferometric measurement methods are based on the detection of the OPD Δz . In most commercial LCI systems, one arm length of the interferometer is scanned and the corresponding interference pattern is recorded time sequentially [5, 7]. The first section shows an evaluation with phase accuracy based on the lock-in technique [18, 19]. Then the limitations of the evaluation are discussed by real measurements with the

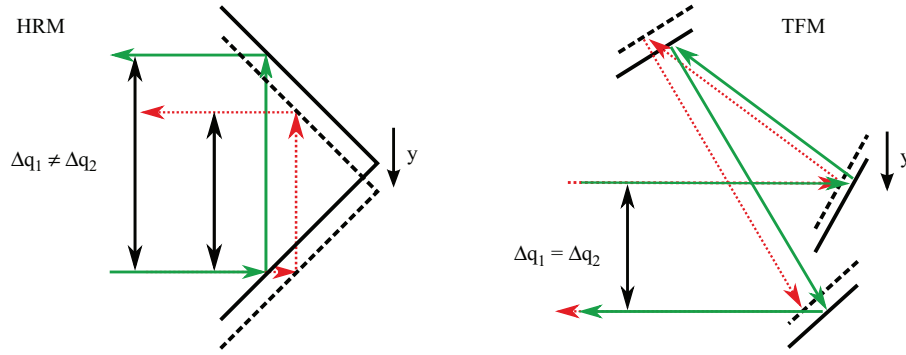


Figure 5. Reflection of a single ray by a HRM and a TFM. If the HRM is displaced in the y direction the ray (dotted) is reflected with a different lateral shear distance ($\Delta q_1 \neq \Delta q_2$). In case of the TFM is lateral shear distance stay constant ($\Delta q_1 = \Delta q_2$).

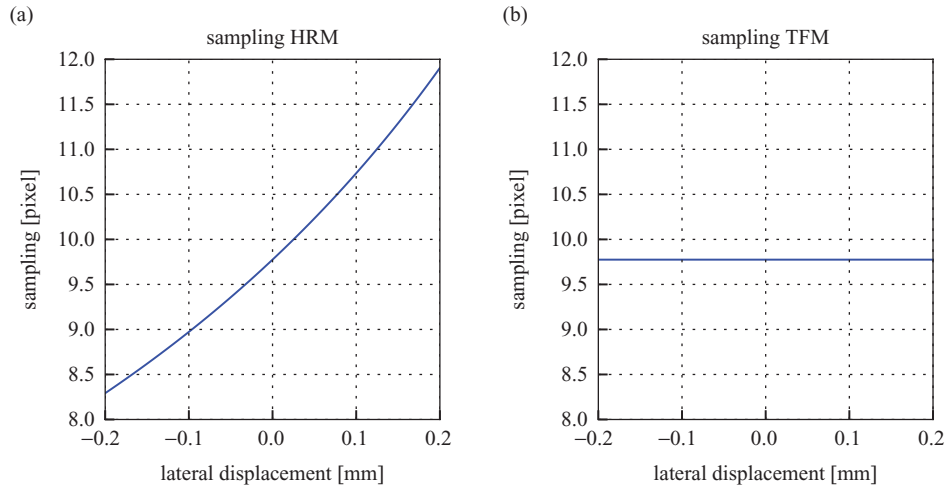


Figure 6. Sampling dependency on a lateral displacement in y direction in case of a HRM (a) and a TFM (b).

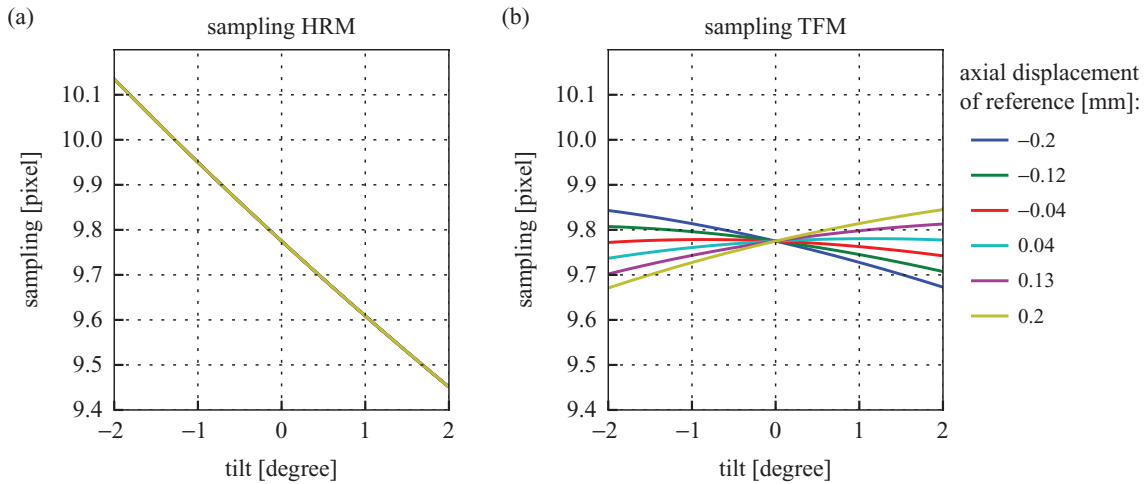


Figure 7. Sampling dependency on a tilt angle of the mirror group in case of a HRM(a) and a TFM(b).

presented setup. Finally, the evaluation procedure is also verified by a commercial scanning WLI sensor.

4.1. Signal processing

In interferometric metrology, the OPD is defined as follows, with the arm lengths z_R and z_O of the reference and the object respectively:

$$\Delta z = 2(z_O - z_R). \quad (10)$$

Caused by the tilted wavefront in the discussed system, the phase on the detector varies along the spatial axis y (see also section 2) which is equivalent to a variation of z_R , so that the OPD is given by:

$$\Delta z = 2z_O - 2z_{R0} + y \times \sin(\alpha), \quad (11)$$

where the basic length of the reference arm is represented by z_{R0} . To obtain the signal of the discussed system the two beam interference term I_{tb} [15]:

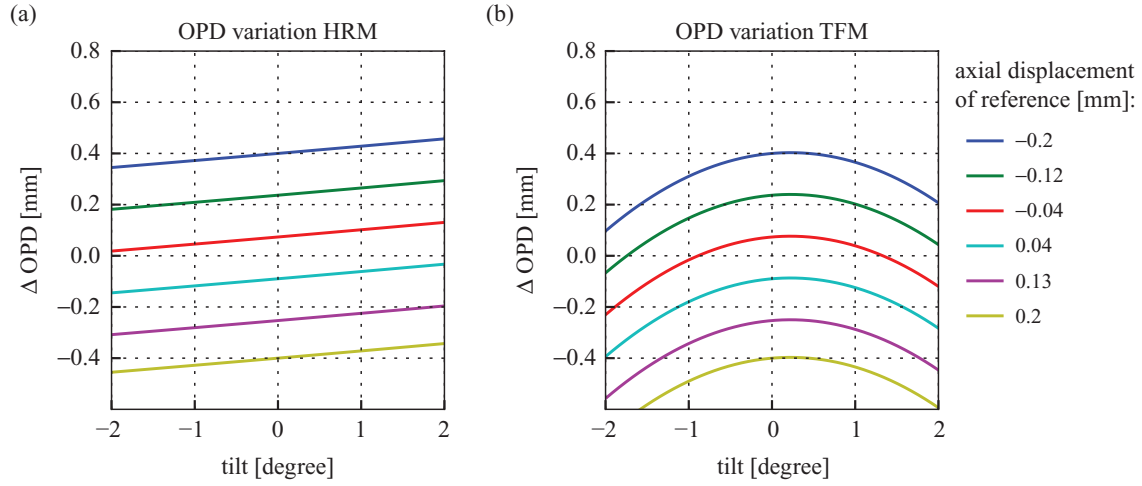


Figure 8. OPD dependency on the tilt angle and the axial position in case of a HRM (a) and a TFM (b).

$$I_{ib}(\Delta z, k) = I_R + I_O + 2(I_R I_O)^{1/2} \times \cos(k \times \Delta z + \phi) \quad (12)$$

must be integrated over a spectral range $\Delta\nu$, with the assumption of a constant intensity distribution of the spectrum and the relation:

$$\nu = \frac{c}{\lambda}. \quad (13)$$

Hereby, c is the speed of light and λ the wavelength. It follows analytically:

$$\begin{aligned} I_{LC}(\Delta\nu, \Delta z, \nu_0) &= \frac{1}{\Delta\nu} \int_{\nu_0 - \Delta\nu/2}^{\nu_0 + \Delta\nu/2} I_{ib}(\Delta z, k) d\nu \\ &= I_R + I_O \left[1 + \text{sinc}\left(\frac{\Delta z \times \Delta\nu}{c}\right) \cos\left(\frac{2\pi \times \nu_0 \times \Delta z}{c} + \phi\right) \right], \end{aligned} \quad (14)$$

with the central frequency ν_0 , the bandwidth $\Delta\nu$ of the spectrum and a global start phase ϕ , which results from possible aberrations of the system. The prefactor $1/\Delta\nu$ is required to scale the DC intensity of the signal to $I_R + I_O$. With equations (11) and (13), the signal can be modified to:

$$\begin{aligned} I_{LC}(\Delta z, \Delta k, k_0) &= I_R + I_O + 2(I_R I_O)^{1/2} \\ &\times \text{sinc}\left\{ [2z_O - 2z_{R0} + y \times \sin(\alpha)] \frac{\Delta k}{2\pi} \right\} \\ &\times \cos\{k_0 [2z_O - 2z_{R0} + y \times \sin(\alpha)] + \phi\}. \end{aligned} \quad (15)$$

The central wavenumber is k_0 and the spectrum width is Δk . If the phase ϕ is equal to zero, the position of the center of gravity (COG) and the zero-order interference fringe are located at exactly the same position. However, in real systems the phase ϕ is not equal to zero [16, 17]. To achieve high position resolutions, the zero-order interference fringe is rather evaluated than the COG of the envelope. Therefore, we accomplished a so called ‘lock-in evaluation’ [18, 19]. Figure 9 presents a raw signal of one camera pixel line and the corresponding region of interest (ROI) of the wavelet.

In a first step a moving average filter is applied on the raw signal to remove the DC offset. As it can be seen in figure 10(a), the envelope of the signal I_{DC} is deformed due to inhomogeneous illumination of the pupil. This deformation can be corrected by dividing the amplitude term by $2(I_R I_O)^{1/2}$.

After these steps the unwanted terms $I_R + I_O$ and $2(I_R I_O)^{1/2}$ of equation (15) are removed and the envelope and frequency, carrying the object information, are extracted. The intensities which are needed for this step, were previously recorded by reference measurements with a blocked reference and object arm respectively. The modified intensity I_E has a symmetrical envelope, as shown in figure 10(b) after these steps.

In the following, the signal frequency corresponding to the wavenumber k_0 is determined by the help of the Fourier transform. If the frequency is known, then the modified interference signal is multiplied with a so called complex lock-in function with the same wavenumber k_0 :

$$f_{L-I} = \exp(-ik_0 \times \Delta z). \quad (16)$$

Afterwards, a phase stable low-pass filter is applied. This yields to the intermediate result I_{filtered} depicted in figure 11. The envelope $E(\Delta z)$ of the interferogram can be calculated by the absolute square of I_{filtered} :

$$E(\Delta z) = 2[\Re(I_{\text{filtered}})^2 + \Im(I_{\text{filtered}})^2]^{1/2}. \quad (17)$$

Then the COG of the envelope $E(\Delta z)$ is calculated. Figure 12 shows the envelope and the calculated COG position z_{COG} .

This value will be used later as the initial point for the determination of the OPD Δz , which is linear proportional to the relative object position z_O (see equation (10)). For this step, the phase ϕ between the lock-in function f_{L-I} and the signal I_E has to be calculated. This is done by summing up the imaginary and real values of the function I_{filtered} and using the arctan2 function:

$$\phi = \arctan 2 \left[\sum \Im(I_{\text{filtered}}), \sum \Re(I_{\text{filtered}}) \right]. \quad (18)$$

The sum is needed to dissolve the discretisation of the data and is legal due to constant phase difference between the lock-in function f_{L-I} and the signal I_E across the data set. Additional the phase ϕ_{COG} of the function f_{L-I} at the position z_{COG} is calculated by:

$$\phi_{\text{COG}} = k_0 \times z_{\text{COG}} \mod 2\pi. \quad (19)$$

Afterwards the distance Δz_d of the nearest zero-phase-crossing position $z_{\phi 0, \text{lock-in}}$ of the lock-in function f_{L-I} to the position z_{COG} is calculated by:

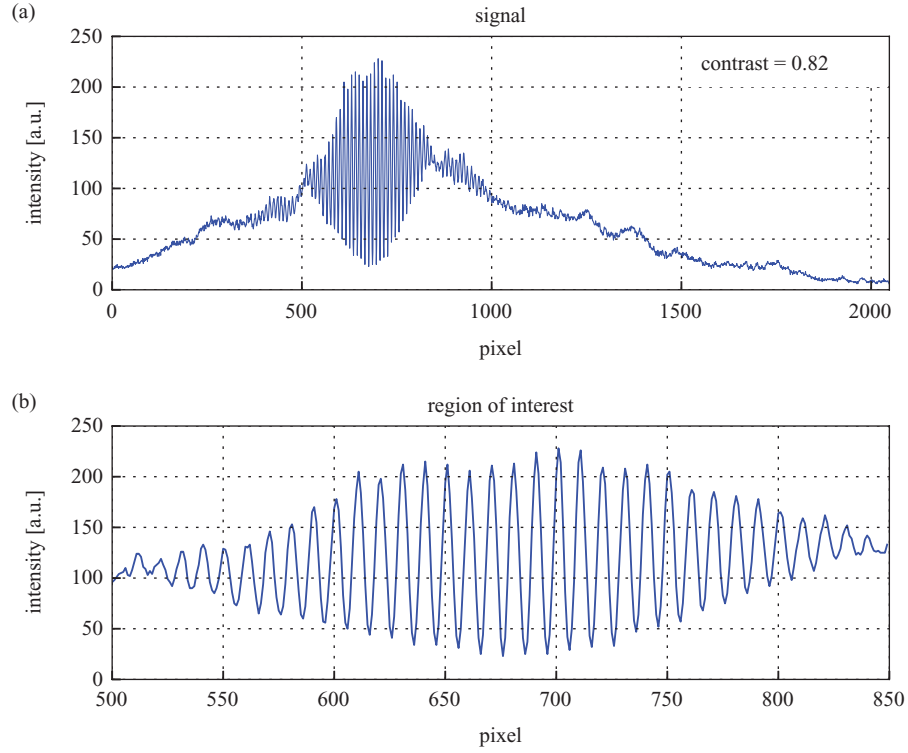


Figure 9. Detected low coherence interferogram of one camera pixel line (a) and the ROI of the wavelet (b).

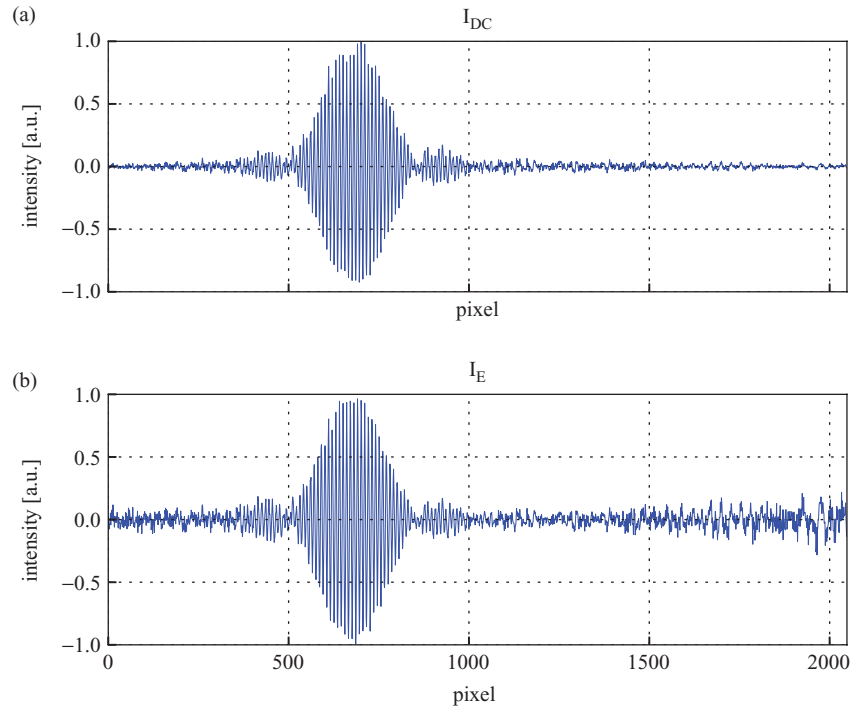


Figure 10. (a): Signal after applying of a moving average filter (b): Signal with a symmetric envelope after dividing through the amplitude term $2(I_R I_O)^{1/2}$.

$$\Delta z_d = \begin{cases} -\frac{\phi_{COG}}{k_0} & \text{if } \phi_{COG} \leq \pi \\ \frac{2\pi - \phi_{COG}}{k_0} & \text{if } \phi_{COG} > \pi. \end{cases} \quad (20)$$

Figure 13 shows how the nearest zero-phase-crossing position $z_{\phi 0, \text{lock-in}}$ is determinate for these two cases.

It follows for the position $z_{\phi 0, \text{lock-in}} = z_{COG} + \Delta z_d$. The nearest zero-phase-crossing position $z_{\phi 0}$ of the signal to the position $z_{\phi 0, \text{lock-in}}$ is determined by:

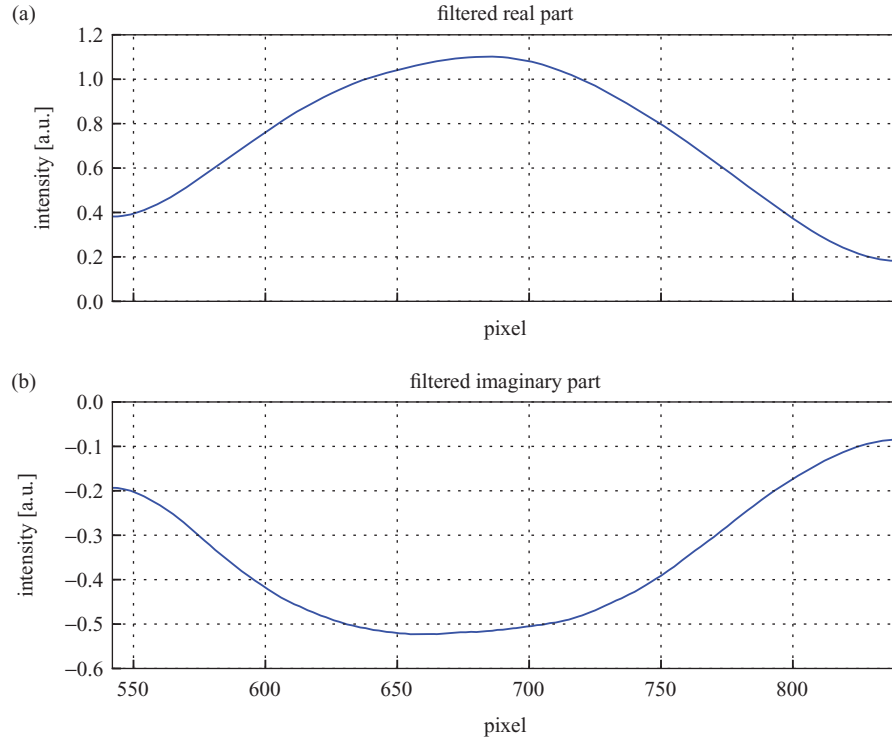


Figure 11. Real part (a) and imaginary part (b) of the low-pass filtered intermediate result I_{filtered} .

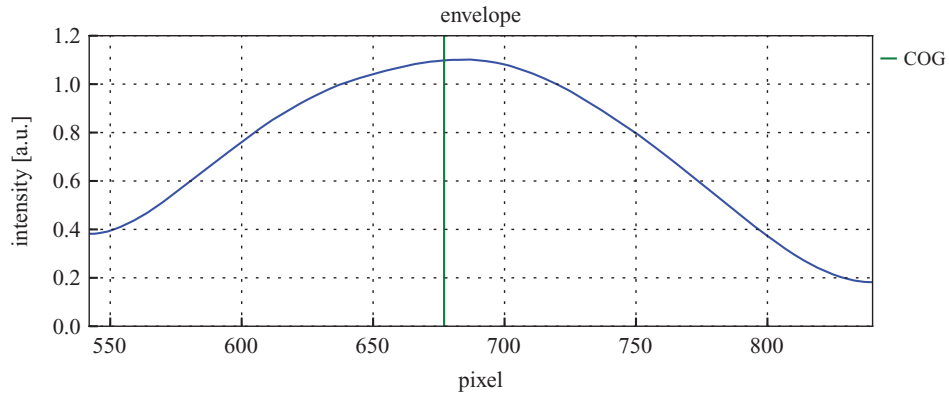


Figure 12. Envelope of the wavelet and the corresponding center of gravity position.

$$z_{\phi 0} = z_{\phi 0, \text{lock-in}} + \frac{\phi}{k_0}. \quad (21)$$

Since the arctan2, used in equation (18), is only defined in the interval $(-\pi; \pi]$ the phase error can be calculated in the range half of a wavelength. Therefore, it has to be checked in a final step, if the distance between $z_{\phi 0}$ and z_{COG} is greater than a half wavelength, if so the object position z_O has to be corrected by $\pm \pi/k_0$:

$$z_O = \begin{cases} z_{\phi 0} + \frac{2\pi}{k_0} & \text{if } z_{\text{COG}} - z_{\phi 0} > \frac{\pi}{k_0} \\ z_{\phi 0} - \frac{2\pi}{k_0} & \text{if } z_{\text{COG}} - z_{\phi 0} < -\frac{\pi}{k_0} \\ z_{\phi 0} & \text{if } -\frac{\pi}{k_0} \leq z_{\text{COG}} - z_{\phi 0} \leq \frac{\pi}{k_0} \end{cases} \quad (22)$$

In case one and two of figure 14 the calculated $z_{\phi 0}$ position is unequal to the nearest fringe order of the COG. Therefore the

final object position z_O has to be corrected by the factor $2\pi/k_0$. If $z_{\phi 0}$ is the nearest fringe order to the COG, this correction is not needed (case 3).

In figure 15 a region of interest of the detected, evaluated wavelet is shown. Finally, the COG z_{COG} and lock-in position z_O are marked in this figure.

4.2. Limitation

To evaluate the difference between the presented lock-in evaluation and a simple evaluation of the COG, a mirror has been measured 100 times at the same position. Afterwards the mirror is moved by $1 \mu\text{m}$ in the direction of the optical axis by means of a piezo actuator. This measurement has been repeated three times. In figure 16, the result of the lock-in evaluation as well as the COG evaluation are shown.

When looking at the graph, it is obvious, that the difference of the result between the lock-in and the COG evaluation

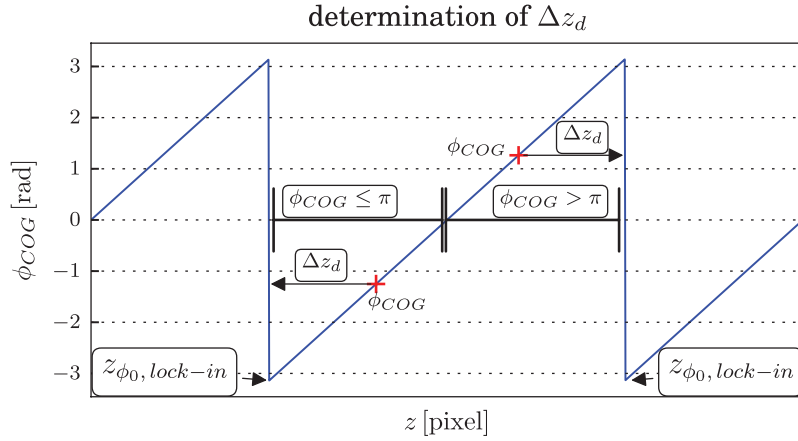


Figure 13. Illustration of the connection between Δz_d and ϕ_{COG} to calculate $z_{\phi 0, lock-in}$.

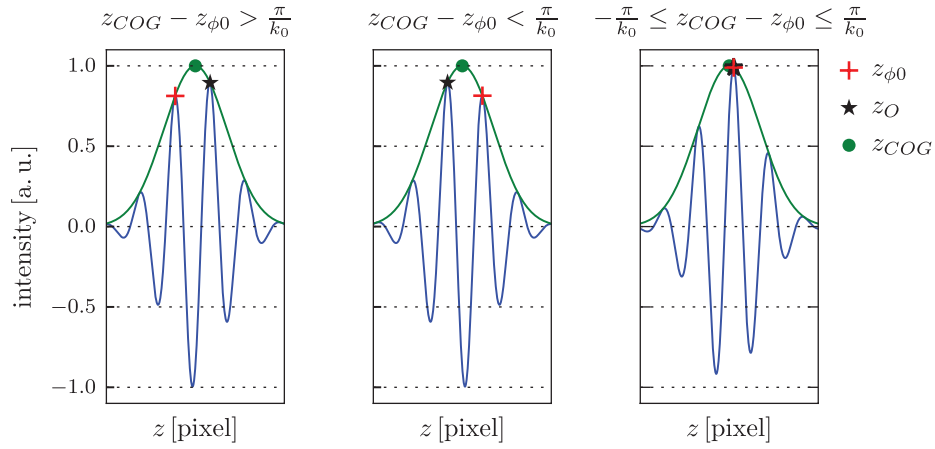


Figure 14. Three wavelets with different phases. Case one and two shows a wrong calculated fringe order and must be corrected to the nearest one to the COG.

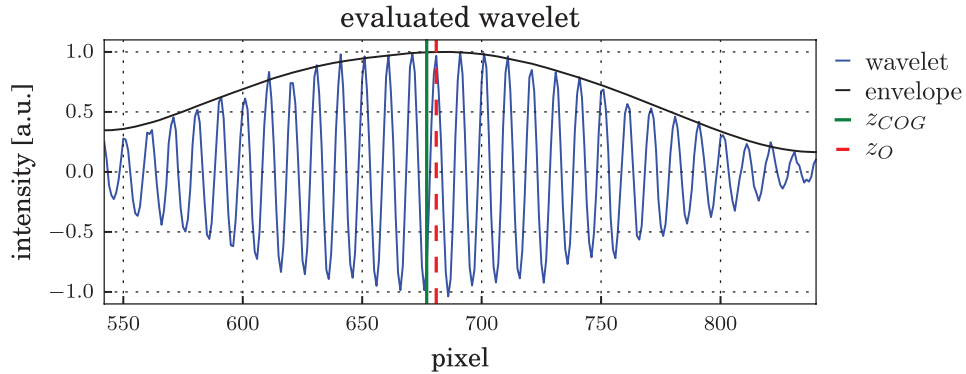


Figure 15. Region of interest of an evaluated wavelet with the envelope, COG position z_{COG} and lock-in position z_O .

does not remain constant for the different axial positions of the object. This can be explained by the aberrations across the pupil plane and the camera chip respectively. However, there is a potential to calibrate this offset, so that the speed of the evaluation is dramatically increased. The feasibility of such a calibration has to be studied in detail in further work. Furthermore, it has to be noticed, that the standard deviation of the evaluated position by the lock-in evaluation is much smaller compared to the one of the COG evaluation. The mean standard deviation of the lock-in evaluation is about 0.088 pixel, whereas the one of the COG evaluation is about 0.483 pixel.

The shown signal evaluation procedure has also its limitations, like the most signal evaluation routines. As previously described, the algorithm is only in the position to find the zero-phase-crossing next to the COG. This leads to unwrapping errors resulting in wrong height values when the COG is located to a position where the phase ϕ of the signal is out of the interval $(-\pi; \pi]$. If this happens, an object position with an offset of $n \times \lambda$, $n \in \mathbb{N}$ is detected. Figure 17 shows a measurement similar to the one depicted in figure 16 but with an axial object position leading to wavelets at an other position on the camera. There the aberrations are close to $\lambda/2$, as

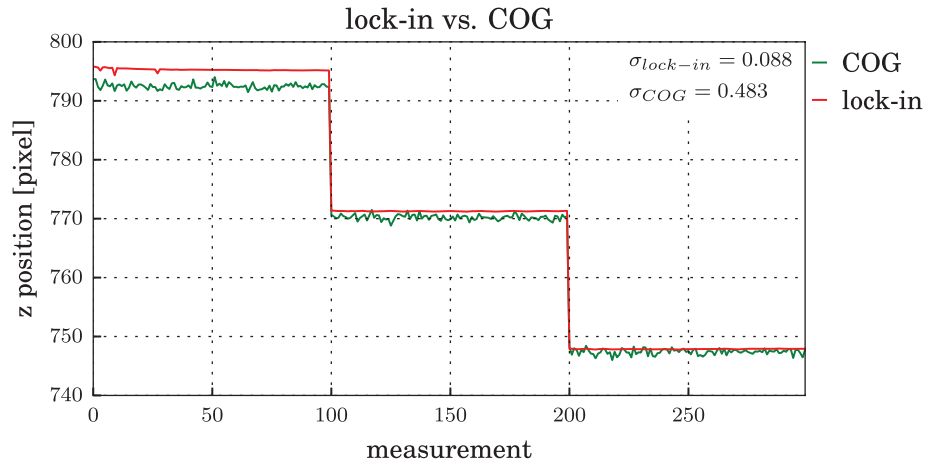


Figure 16. Comparison between the COG- and the lock-in evaluation by repeated measurement of a mirror at three different axial positions with 1 μm separation.

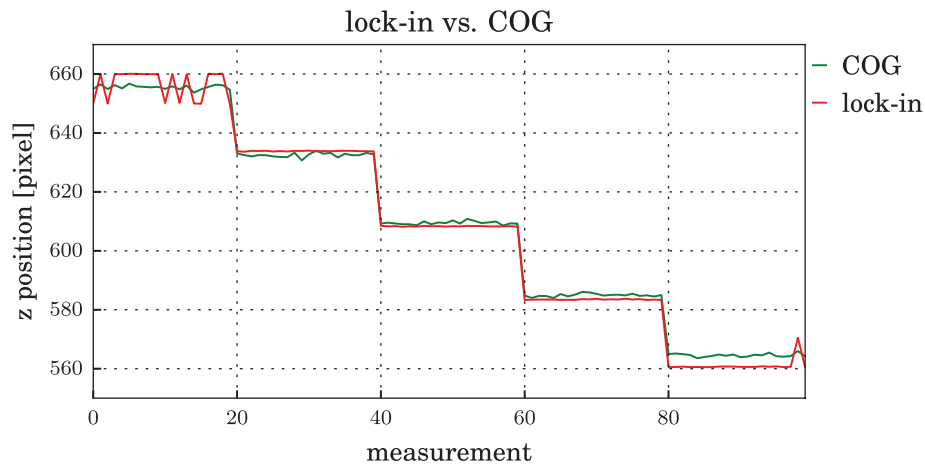


Figure 17. Comparison between the COG- and the lock-in evaluation. At the measurements 0–20 and 80–100 the phase of the signal at the COG was close to π leading to unwrapping errors resulting in a spiky lock-in position.

it can be seen clearly by the unwrapping errors, resulting in a signal phase close to π at the COG. At the measurement positions 0–20 and 80–100 of figure 17 the COG position remains nearly constant with a standard deviation $\sigma = 0.57$ pixel, while the lock-in positions vary symmetrically to the COG position with $\sigma = 2.20$ pixel. At the measurement positions 20–80, the evaluation results without unwrapping errors and the object height is reconstructed very smooth with $\sigma = 0.11$ pixel for the lock-in and $\sigma = 0.52$ pixel for the COG evaluation. Nevertheless, the full potential of the lock-in evaluation gets clear while looking at the standard deviations of both evaluation procedures in case of less unwrapping errors.

The existence of those errors shows the importance of a well optimized optic design. A design with a higher NA would lead to a smaller spot on the object, yielding in less object influences caused by different object heights inside the spot. The inhomogeneous illumination of the sensor also turned out to have a negative effect on the signal evaluation, since the envelope is quite deformed. This could be improved in further work by the use of a top-hat shaping optical element. Also a less extended signal envelope would have a positive effect on the precision of the COG evaluation and therefore also on the lock-in evaluation. A possibility of shrinking the envelope is

either to increase the bandwidth of the lightsource or the tilt of the reference wavefront.

4.3. Verification of the signal processing

To show the potential of the algorithm a commercial sensor has been used for verification. The Mahr Surf WS1 is based on a scanning Mirau-interferometer with objective lenses fabricated by Leica. A piezo actuator has scanned the Leica N-Plan 50x/0.50 MIRAU objective lens over a range of approximately 4 μm with 500 steps. As object the groove with a height of 0.756 μm of the Halle depth calibration standard [21] was measured. Figure 18 illustrates the result of the COG and lock-in evaluation. The calculated height of 0.761 μm is within the given specifications (minimum = 0.736 μm , maximum = 0.776 μm) by the Physikalisch-Technische Bundesanstalt (PTB) [22]. It is also recognizable that both evaluation results has a height offset, resulting from the phase ϕ between the COG and the nearest zero-phase-crossing peak of the wavelet. As already discussed in section 4.2 the standard deviation of the lock-in evaluation is less than the one of the COG evaluation. This measurement

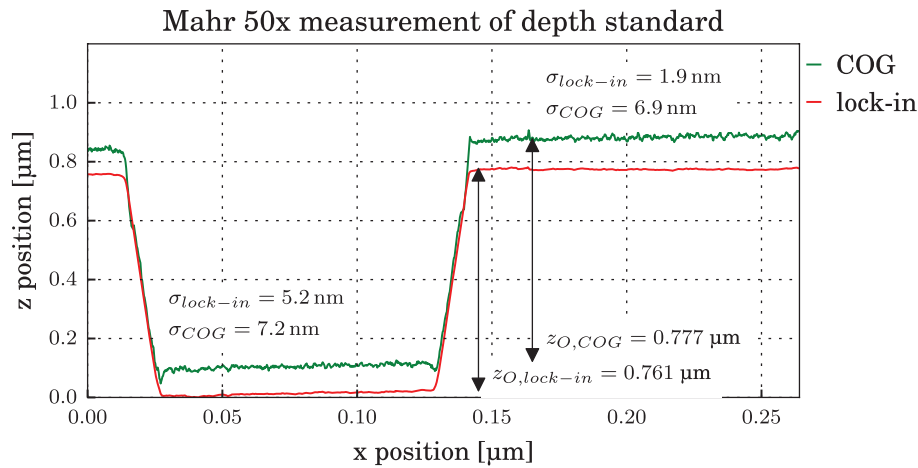


Figure 18. Measurement of the 0.756 μm groove depth of the Halle depth calibration standard KNT 4080/03 (mean = 0.756 μm , minimum = 0.736 μm , maximum = 0.776 μm). Evaluated lock-in height is 0.761 μm and COG height is 0.777 μm . The standard deviation of each height level is also given.

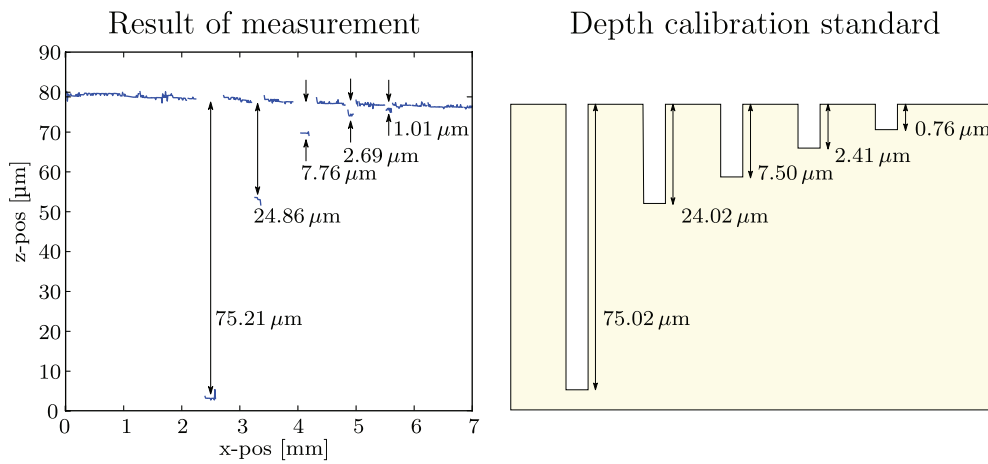


Figure 19. Measurement of the topography of the Halle depth calibration normal.

shows clearly the potential of the lock-in technique for a scanning WLI on a cooperative surface.

5. Experimental verification

Finally, the suitability of this sensor for surface metrology tasks is demonstrated. First of all, the system was calibrated by a GUM Type A calibration [20], to transfer the detected pixel position into a metric scale. The calibration procedure has been done by measuring a mirror position several times at different axial positions. The so found calibration factor is 0.046 $\mu\text{m}/\text{pixel}$. In order to get an estimate about the achieved measurement uncertainty, the standard deviation of 100 repeated measurements at one stationary mirror position has been determined. The results of these measurements, executed at different axial positions in the full measurement range, are depicted in figure 16. Multiplying them by the obtained calibration value result in deviations of 4.047 nm for the lock-in and 22.218 nm for the COG evaluation. These values are in the same range than the standard deviations of the measurements using the Mahr WLI (figure 18).

For a first estimation of the measurement accuracy, a Halle depth calibration standard [21] with grooves from 0.76 μm to

75.02 μm was measured. Figure 19 shows the result of this measurement and the reference depths given by the PTB [22]. The evaluation of the groove depths was done according to the industrial standard DIN EN ISO 5436-1. As it can be seen, the measured depths are different to the reference depths. A systematical bias can not be observed, because the difference does not show any dependency of the evaluated depth. In the resulting plot of figure 19 one step height of the standard results in a spiky plane, caused by unwrapping errors discussed in the previous section 4.2. It is obvious that those errors distort the reconstructed groove depths. Our experience with the moving stage is that the spindle accuracy of the vertical axis is about 200 nm by moving in the horizontal axis. This uncertainty is less than the one caused by the phase unwrapping errors ($\approx 450 \text{ nm}$) shown in figure 17. Moreover, lines are fitted for the depth evaluation by a least square fit into the different height levels. So the greater uncertainty leads to a greater impact on the evaluated groove depth. An estimate for the measurement accuracy is obtained by the maximum difference between the measurements of the Halle depth calibration standard and its reference values from the calibration sheet. In the current implementation, a maximum difference of 0.8 μm has been measurement, which is mainly influenced

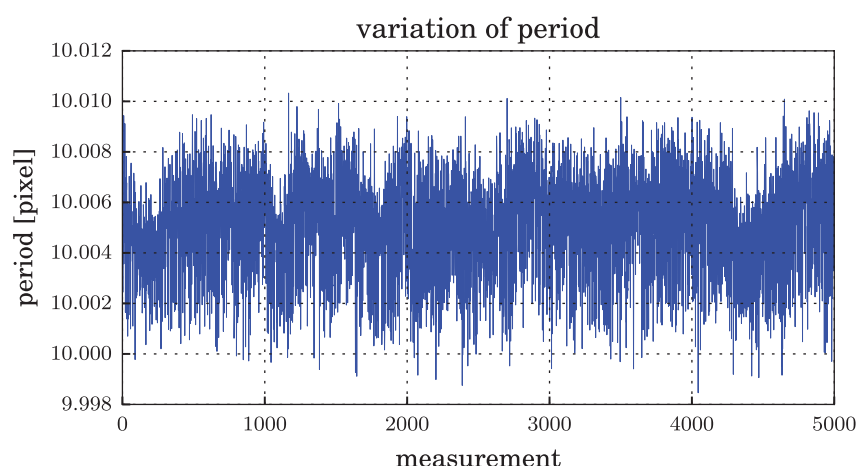


Figure 20. Detected period of the wavelets in a vibrating environment by 5000 measurements with a maximum period variation of 0.012 pixel.

by an inhomogeneous illumination of the pupil plane as well as the uncorrected phase steps. Improving these conditions is expected to highly reduce the overall accuracy.

As described in section 3.1 the system is supposed to guarantee a stable signal frequency. In the measurement of figure 20, the robustness of the system is experimentally demonstrated. For this purpose, a vibrating cell phone was mounted directly on top of the TFM and 5000 measurements with a constant object position have been detected. After subtraction of the constant part of the signal, the period of the wavelets has been evaluated with subpixel precision. The result shows that the period of the signals only varies by 0.012 pixel, showing that the aim of a constant signal period is fulfilled.

6. Conclusion

In this paper a new type of single-shot low-coherence interferometry point sensor was introduced and demonstrated by a laboratory optical setup. The key component is a three faceted mirror in the reference arm which generates a virtual reference field point. In this telecentric arrangement, the coherent field point is collimated as a planar tilted wavefront. In the pupil position, it interferes with the object wavefront where a spatial modulated interferogram is detected by a camera chip. By using a short coherent lightsource, a LCI wavelet is acquired in one camera frame. The TFM guarantees a stable signal frequency due to the monolithic fabrication of the mirror group which guarantees a constant lateral shear distance.

The signal evaluation of the presented point sensor is derived from a lock-in evaluation of common white light interferometers. In a first measurement of a depth calibration standard, the groove depths were reconstructed. This measurement shows the suitability as a surface measurement sensor. In principle, it is able to detect the different groove depths, whose positions are reconstructed with unwrapping errors. Nonetheless, we have to investigate the signal processing to get rid of the unwrapping errors. To avoid wrong height values, the sensor can be improved as well as the signal evaluation. On the sensor side the detected wavelet appears

more symmetric and narrow, when the sensor illumination is more homogeneous and with a broader spectral width. There is also the possibility to use a heterodyne signal evaluation by inserting a second light source with a slightly different spectrum as shown in [11] or the use of a frequency based evaluation like demonstrated in [17, 23, 24].

In this paper the proof of concept of this sensor approach was demonstrated. It is obvious that this single-shot point sensor can be extended to a single-shot line sensor, realized by the use of cylindrical objective lenses. One camera axis corresponds to the focused line on the object and the other shows the interferograms for each object point of the line. The full potential of this sensor concept for fast in-line inspection will be reached by further optimization and extension to a single-shot line sensor.

References

- [1] Yang Z, Bielke A and Häusler G 2016 Better three-dimensional inspection with structured illumination: speed *Appl. Opt.* **55** 1713–19
- [2] Häusler G and Lindner M W 1998 ‘Coherence radar’ and ‘spectral radar’—new tools for dermatological diagnosis *J. Biomed. Opt.* **3** 21–31
- [3] Fercher A F, Hitzinger C K, Kamp G and El-Zaiat S Y 1995 Measurement of intraocular distances by backscattering spectral interferometry *Opt. Commun.* **117** 43–8
- [4] Endo T, Yasuno Y, Makita S, Itoh M and Yatagai T 2005 Profilometry with line-field Fourier-domain interferometry *Opt. Exp.* **13** 695–701
- [5] Kino G S and Chim S S C 1990 Mirau correlation microscope *Appl. Opt.* **29** 3775–83
- [6] Dresel T, Häusler G and Venzke H 1992 Three-dimensional sensing of rough surfaces by coherence radar *Appl. Opt.* **31** 919–25
- [7] Deck L and de Groot P 1994 High-speed noncontact profiler based on scanning white-light interferometry *Appl. Opt.* **33** 7334–38
- [8] Hering M, Herrmann S, Körner K and Jähne B 2006 Line-profiling white-light interferometers for in-line industrial inspection *SPIE Newsroom* (doi: 10.1117/2.1200606.0291)
- [9] Hering M, Herrmann S, Banyaya M, Körner K and Jähne B 2006 One-shot line-profiling white light interferometer with

- spatial phase shift for measuring rough surfaces *Proc. SPIE* **6188** 61880E
- [10] Hering M, Körner K and Jähne B 2009 Correlated speckle noise in white-light interferometry: theoretical analysis of measurement uncertainty *Appl. Opt.* **48** 525–38
- [11] Depiereux F, Lehmann P, Pfeifer T and Schmitt R 2007 Fiber-optical sensor with miniaturized probe head and nanometer accuracy based on spatially modulated low-coherence interferogram analysis *Appl. Opt.* **45** 3425–31
- [12] Körner K, Berger R and Osten W 2015 Method and arrangement for robust interferometry for detecting a feature of an object *US Patent* 8,934,104 B2
- [13] Bauerschmidt M 1965 Rechnerische Bestimmung von Spiegelfolgen und Spiegelprismen sowie deren Eigenschaften *PhD Dissertation* TH Ilmenau, Ilmenau
- [14] LT ULTRA www.lt-ultra.de/
- [15] Bass M, van Stryland E, Williams D and Wolfe W 1995 *Handbook of Optics* (New York: McGraw-Hill)
- [16] Pavlíček P and Häusler G 2005 White-light interferometer with dispersion: an accurate fiber-optic sensor for the measurement of distance *Appl. Opt.* **44** 2978–83
- [17] Pförtner A and Schwider J 2001 Dispersion error in white-light Linnik interferometers and its implications for evaluation procedures *Appl. Opt.* **40** 6223–28
- [18] Fleischer M, Windecker R and Tiziani H J 2000 Fast algorithms for data reduction in modern optical three-dimensional profile measurement systems with MMX technology *Appl. Opt.* **39** 1290–97
- [19] Masciotti J, Lasker J and Hielscher A 2008 Digital lock-in detection for detection for discriminating multiple modulation frequencies with high accuracy and computational efficiency *IEEE Trans. Instrum. Meas.* **57** 182–9
- [20] ISO/IEC Guide 98-3:2008 1995 Guide to the expression of uncertainty in measurement
- [21] HALLE www.halle-normale.de/
- [22] Physikalisch-Technische Bundesanstalt www.ptb.de/cms/
- [23] Ghim Y S and Davies A 2012 Complete fringe order determination in scanning white-light interferometry using a Fourier-based technique *Appl. Opt.* **51** 1922–8
- [24] de Groot P and Deck L 1995 Surface profiling by analysis of white-light interferograms in the spatial frequency domain *J. Mod. Opt.* **42** 389–401